RSC Advances

PAPER

View Article Online
View Journal | View Issue

Cite this: *RSC Adv.*, 2025, **15**, 24040

Graphene oxide vacancies-assisted low temperature synthesis of graphitic carbon quantum dots for enhanced conductive networks in epoxy composites

Thanayuth Jongrungrotbaworn,†[ab] Rungkiat Nganglumpoon,†[b] Suthasinee Watmanee,[c] Sukkaneste Tungasmita,[d] Ryota Sakamoto[ef] and Joongjai Panpranot *[bgh]

Conventional bottom-up synthesis of graphitic carbon quantum dots (g-CQDs) often requires extended reaction times, high energy input, and specialized equipment, limiting scalability and sustainability. In this study, we present an eco-friendly and energy-efficient method for synthesizing g-CQDs using H_2CO_3 as a carbon precursor at just 72 °C for 1 hour—representing one of the lowest reported synthesis temperatures and shortest reaction times using simple apparatus. Graphene oxide vacancies act as catalytic and nucleation sites, promoting the formation of g-CQDs under these mild conditions. The resulting g-CQD solution exhibits strong yellow photoluminescence, with a maximum emission at 533 nm and excitation-independence across the 320–410 nm range. Upon drying, the g-CQDs spontaneously assemble into a three-dimensional (3D) network, which provides additional functionality when incorporated into g-CQD/graphene nanoplatelet epoxy composites. This strategy not only promotes the sustainable production of g-CQDs but also broadens their potential for use in next-generation nanomaterials and optoelectronic devices.

Received 16th May 2025
Accepted 30th June 2025

DOI: 10.1039/d5ra03471j

rsc.li/rsc-advances

Introduction

Polymer-carbon nanomaterial composites combine the properties of polymers (flexibility, lightweight, processability) with the exceptional electrical, mechanical, and thermal properties of carbon-based nanomaterials such as carbon nanotubes, graphene, and fullerenes. They find applications across diverse industries such as thermal management in electronic modules, and battery systems,[1] superconductivity for electrical and anti-static applications,[2,3] flexible electronics,[4] biosensors, *etc.* Thanks to their lightweight nature, large specific surface area, excellent thermal and electrical conductivity, and high mechanical strength, composite materials made of epoxy resin and graphene nanoplatelets (GNPs) are highly sought after for specific applications, where efficient heat and electricity management is critical.[5–9]

Efficient thermal and electrical conduction in polymer composites necessitates the formation of highly continuous conductive networks, typically achievable at high loadings of GNPs.[10,11] However, the graphitic structure of GNPs tends to form irreversible agglomeration due to strong van der Waals interactions, posing challenges to achieving uniform dispersion.[12–14] The incorporation of various carbon materials, such as GNPs, carbon nanotubes (CNTs), and graphene oxide (GO), has demonstrated a synergistic effect of hybrid fillers, facilitating the creation of interconnected conductive networks that significantly enhance the thermal and electrical properties of polymer composites.[10,14–16]

New class of carbon nanomaterials, represented by graphene quantum dots (GQDs), carbon quantum dots (CQDs), and CQDs with graphitic character, called graphitic carbon quantum dots (g-CQDs).[17] Due to their unique properties such as biocompatibility, low toxicity, small bandgap, confinement effects, and high solubility, these carbon nanomaterials have been widely explored for

[a]*MSc. Program in Research for Enterprise, Faculty of Pharmaceutical Sciences, Chulalongkorn University, Thailand*

[b]*CrystalLyte Co., Ltd, Research Unit 904, Faculty of Engineering, Chulalongkorn University, Bangkok, 10330, Thailand. E-mail: joongjai.p@chula.ac.th*

[c]*Department of Chemical Engineering, Faculty of Engineering, Kasetsart University, Bangkok, 10900, Thailand*

[d]*Department of Physics, Faculty of Science, Chulalongkorn University, Bangkok, 10330, Thailand*

[e]*Department of Chemistry, Graduate School of Science, Tohoku University, 6-3 Aramaki-Aza-Aoba, Aoba-ku, Sendai, 980-8578, Japan*

[f]*Division for the Establishment of Frontier Sciences of Organization for Advanced Studies at Tohoku University, 2-1-1 Katahira, Aoba-ku, Sendai, 980-8577, Japan*

[g]*Department of Chemical and Petroleum Engineering, Faculty of Engineering, Technology and Built Environment, UCSI University, Cheras, 56000, Kuala Lumpur, Malaysia*

[h]*Center of Excellence on Catalysis and Catalytic Reaction Engineering, Department of Chemical Engineering, Faculty of Engineering, Chulalongkorn University, Bangkok, 10330, Thailand*

† Equal contribution.

diverse applications, including drug delivery, bioimaging, sensing, ultraviolet photo-detectors, photocatalysis, batteries, and cement enhancement.[17–23] Recently, carbon nanomaterials have garnered significant interest as electrically and thermally conductive fillers in polymer matrices. For examples, Seibert *et al.*[24] synthesized GQDs from charcoal using sulfuric and nitric acids and incorporated them into epoxy composites. Their study demonstrated that GQDs enhanced the thermal conductivity of the epoxy by 144% and improved its toughness by 260%, attributed to the size effect, surface functional groups, and dispersibility of GQDs. Zhang *et al.*[25] developed a method to further increase the thermal conductivity of epoxy composites by incorporating a hybrid filler of aluminum nitride (AlN) and modified GQDs (D-GQDs). In their study, GQDs were synthesized by pyrolyzing citric acid at 200 °C for 2 h, then modified with polyetheramine (D400), enriching their edges with amino groups. Their result showed that the thermal conductivity of AlN-epoxy was 0.83 W (m K)$^{-1}$, while the hybrid filler system of AlN/D-GQDs in epoxy resin achieved an enhanced thermal conductivity of 1.31 W (m K)$^{-1}$, facilitated by the good thermally conductive network of D-GQDs. Additionally, the electrical conductivity of AlN/D-GQDs-epoxy increased compared to AlN-epoxy, which the authors attributed to the polar hygroscopic functional groups present in D-GQDs.

The bottom-up synthesis of g-CQDs typically involves the chemical assembly of small organic molecules, which enables precise size control and minimizes defect formation therein. However, this approach faces challenges for large-scale production, as it is often time and energy-intensive, has heavy environmental impacts, and requires specialized equipment.[26–29] In this study, we propose a novel, green, and energy-efficient approach for synthesizing g-CQDs using carbonic acid (H_2CO_3) as a carbon precursor and graphene oxide vacancies as catalytic and nucleation sites under low temperature synthesis. H_2CO_3 can be produced from atmospheric carbon dioxide (CO_2), and the g-CQDs production process in this study is also excellent from the perspective of sustainability.[30] The synthesis of g-CQDs is performed under ambient pressure at temperatures below 100 °C within 1 h reaction time. To explore the merit of g-CQDs that form conductive networks with other carbon nanomaterials, hybrid fillers of GNPs and g-CQDs were incorporated into an epoxy resin matrix. The resulting composites were evaluated for enhancements in both thermal and electrical conductivity.

Experimental

Materials

Chemicals used in g-CQDs synthesis: Ammonium sulfate ($(NH_4)_2SO_4$, 99.5%) was purchased from Thomas Baker (Chemicals) Pvt. Ltd, India. Formic acid (HCOOH, 98–100%) was purchased from Sigma-Aldrich. Hydrogen peroxide was purchased from QreC, New Zealand. GO was purchased from Luoyang Tongrun Nano Technology Co., Ltd, China. Sodium hydrogen carbonate ($NaHCO_3$, 99.5–101.0%) was purchased from KemAus Pty., Ltd, Australia. 1 kDa regenerated cellulose membrane tubing used in dialysis was purchased from Spectrum Lab Ltd, New Zealand.

The GNPs-epoxy composites were created using graphene nanoplatelets (GNPs, particle size of 5–25 μm, thickness average of 15 nm, surface area of 50–80 m^2 g^{-1}, oxygen content <1%) from XG Sciences, Inc., US. Mira MR 178-2A, and Mira MR 178B were employed as epoxy resin, and hardener respectively, both sourced from Miradur Sdn. Bhd., Malaysia.

Synthesis of g-CQDs

First, 100 mg of GO was suspended in 50 mL of an aqueous solution containing 0.4 M $(NH_4)_2SO_4$ and 1.5 M HCOOH, and the mixture was heated to 72 °C. Upon reaching 72 °C, 9.45% (w/v) H_2O_2 was added. The solution was then combined with pre-heated 6.30 g $NaHCO_3$ powder at 72 °C and maintained at this temperature for 1 hour. This process yielded a dark brown g-CQD solution, which was subsequently cooled to room temperature. The g-CQD solution was then dialyzed for 3 days and freeze-dried, resulting in a yellowish-brown, sponge-like material.

Characterization

Transmission electron microscopy (TEM) imaging was performed using a Talos F200X instrument at STREC, Chulalongkorn University. A drop of the g-CQDs solution was deposited onto a copper grid for analysis, and the lattice spacing was measured using ImageJ software. The X-ray diffraction (XRD) pattern of g-CQDs sample was recorded in the 2θ range 10°–80° (scan rate = 0.5 s per step) using a Siemens D5000 diffractometer using nickel filtered Cu Kα radiation. X-ray photoelectron spectroscopy (XPS) analysis was conducted by employing Mg Kα X-ray radiation at 10 kV to determine the surface elemental composition. Raman spectra were performed using a Thermos Scientific DXR3 Raman microscope equipped with a 523 nm excitation laser operating at a power of 500 mW and a 100× objective lens. Photoluminescence (PL) spectra were recorded with a Fluoromax R928P spectrometer, with g-CQDs sample excited at 360 nm. Scanning electron micrographs (SEM) and energy-dispersive X-ray spectroscopy (EDX) analyses of the composites were conducted using a Hitachi S-3400 N to examine the fracture surfaces. Thermal conductivity was measured at room temperature using a laser flash analyzer. Samples were prepared as square-shaped specimens with dimensions of 10 mm × 10 mm and a thickness of 2 mm. Prior to measurement the samples were coated with graphite spray. The analysis followed an in-house method based on ASTM E1464-13. Electrical resistivity was determined using the Van der Pauw method, as described in ref. 31. Measurements were performed with a Keithley 230 programmable voltage source and a Keithley 2182A nanovoltmeter.

Results and discussion

Graphene oxide vacancies-assisted low temperature synthesis of g-CQDs

Here, g-CQDs were synthesized using a simple beaker-type reactor as illustrated in Fig. 1(a). The formation of g-CQDs was achieved *via* a graphene oxide vacancies-assisted low

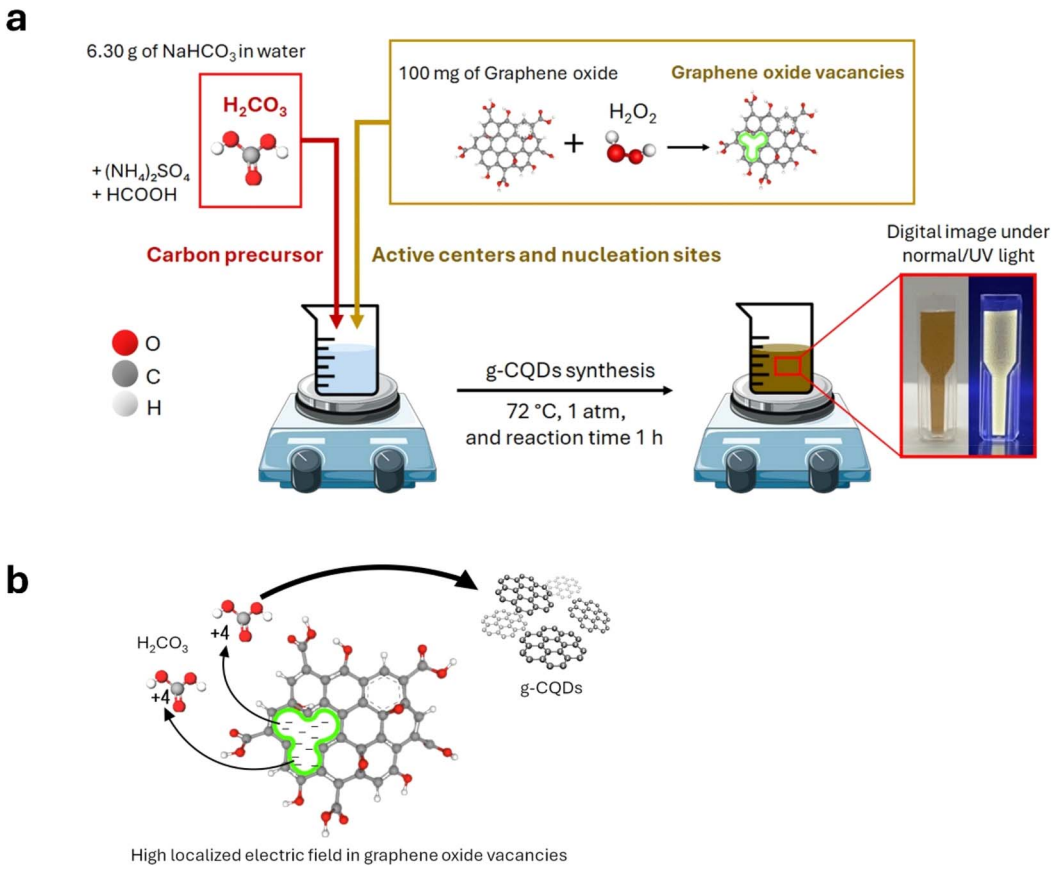

Fig. 1 Schematic illustration of (a) the graphene oxide vacancies-assisted low temperature synthesis of g-CQDs and digital image of the obtained solution under normal light and UV light, (b) interaction between H_2CO_3 and high localized electric field in graphene oxide vacancies catalyzing g-CQD formation.

temperature synthesis. Briefly, a solution containing GO, H_2CO_3, and H_2O_2 was maintained at 72 °C under ambient pressure for 1 h. After the reaction, the solution was dialyzed to remove impurities. The resulting solution appeared brown under normal light and exhibited strong yellow luminescence under UV-light. g-CQDs were formed using H_2CO_3 as a carbon precursor, which was generated by the protonation of bicarbonate ions (HCO_3^-) produced from the dissolution of $NaHCO_3$ in deionized water. The addition of formic acid (HCOOH) facilitated the formation of H_2CO_3. The reaction of GO with H_2O_2 involved the oxidation of the GO structure by hydroxyl radicals ($OH^\bullet$), resulting in the creation of vacancies or defects within the graphene lattice, referred to as graphene oxide vacancies.[32,33] As shown in the schematic model in Fig. 1(b), these defects or vacancies in the graphene oxide structure give rise to localized electronic states with high local charge density near the vacancy sites.[34–36] These sites served as reactive nucleation centers for the growth of g-CQDs and played a crucial role in controlling their size distribution.[36–40] Recent work by Ni, Q., *et al.*[41] demonstrated that functionalization of CQDs with electron-withdrawing groups (EWG) such as $-NO_2$ and $-COOH$, significantly alters their surrounding electronic environment. Their study further showed that these EWG-CQDs can promote the transformation of NiFe-MOFs and facilitate the expansion of interlayer spacing.

Table 1 provides a comprehensive summary of the reaction conditions screened in the synthesis of g-CQDs. The best conditions to produce g-CQDs requires H_2O_2, HCOOH, $NaHCO_3$, and 100 mg of GO (Entry I). H_2CO_3 has proven to be the optimal carbon precursor for this system. HCOOH is employed to facilitate the formation of H_2CO_3. In the absence of HCOOH (Entry II), only weak yellow luminescence was observed under UV light, likely due to the reduced formation of H_2CO_3 in the slightly basic solution. To clarify, the repulsive interaction between bicarbonate anions and graphene oxide vacancies worsens the formation of g-CQDs. Graphene oxide vacancies play a critical catalytic role in the synthesis of g-CQDs when H_2CO_3 is used as the carbon precursor. It is obvious that without H_2O_2, there was almost no g-CQDs formation (Entry III). The oxidation of GO by $OH^\bullet$ radicals is known to generate vacancies or defects within the graphene lattice. This structural disruption is evidenced by the increased D to G band intensity ratio (I_D/I_G) in Raman spectra (Fig. 2). Specifically, the I_D/I_G value increases from 0.94 in GO to 1.03 in GO with vacancies, indicating a reduction in the G band intensity, an effect typically associated with the breakdown of ordered graphitic domains. Graphene oxide vacancies, with its high electron density due to missing carbon atoms, interact actively with H_2CO_3. As a neutral molecule, H_2CO_3 possesses the highest positive charge density on its carbon atom, making it the most effective carbon

Table 1 Various conditions for the synthesis of g-CQDs

	Conditions					
Entry	H_2O_2	HCOOH	$NaHCO_3$	Catalyst	Digital images of g-CQDs solution in normal/UV light	Remark
I	✓	✓	✓	100 mg of GO	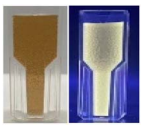	
II	✓	—	✓	100 mg of GO	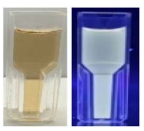	Slighly basic pH of the solution
III	—	✓	✓	100 mg of GO	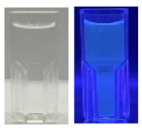	No oxidizing agent
IV	✓	✓	—	100 mg of GO		No carbon precusor
V	✓	✓	✓	10 mg of GO	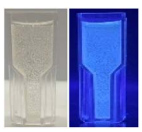	Catalyst decreased
VI	✓	✓	✓	100 mg of graphite	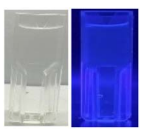	Non-oxdizing catalyst

precursor for this synthesis. While H_2O_2 is sufficient to form vacancy sites in GO, the overall efficiency of CQD production also depends on the formal charge of the carbon atom in the precursor molecule. This is due to the highly localized electric field[42,43] present at the GO vacancy sites, which electrostatically favor the adsorption of highly electropositive species. For instance, the carbon atom in H_2CO_3 carries a formal charge of +4, while in HCOOH it is +2. Consequently, H_2CO_3 demonstrates significantly higher reactivity toward GO vacancies, resulting in superior CQDs yield. On the other hand, $NaHCO_3$ is an ineffective carbon source because HCO_3^- is an anionic species and is electrostatically repelled by the negatively charged active sites. In such alkaline conditions, CQDs are likely formed only *via* hydrolysis of HCO_3^- to H_2CO_3, a reaction

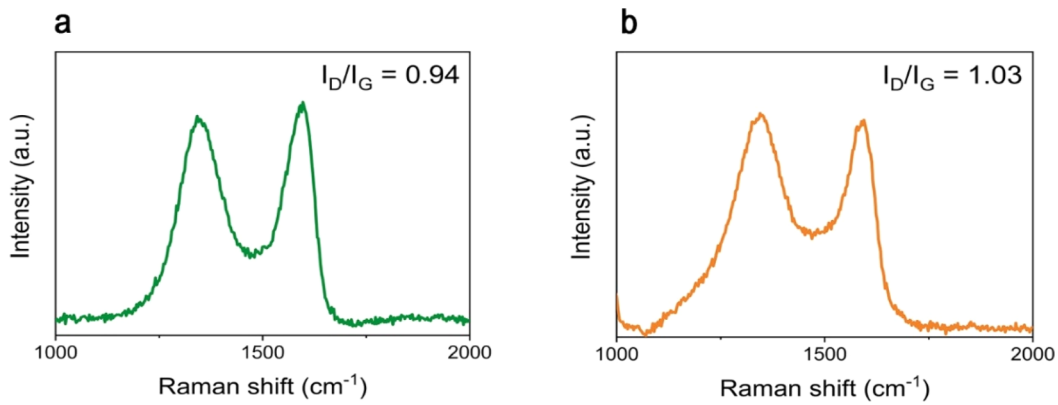

Fig. 2 Raman spectra of (a) the original graphene oxide (b) GO after reaction with H_2O_2 (forming graphene oxide vacancies).

that is thermodynamically disfavored at high pH.[44] Thus, the equilibrium concentration of H_2CO_3 is substantially lower compared to the acidic environment created by direct HCOOH addition, leading to a notably poorer CQD formation performance.

To better understand the catalytic role of GO in the presence of H_2O_2, as opposed to its function as a precursor in a top-down synthesis approach,[45–47] solutions without $NaHCO_3$ were examined to enhance oxidation conditions (Entry IV). These conditions were designed to align more closely with the top-down approach. However, the resulting solution showed almost no luminescence under UV light, suggesting that the top-down conversion of GO into g-CQDs necessitates stronger oxidizing agents such as sulfuric and nitric acids.[45,48] To elaborate, if the g-CQDs were formed *via* a top-down synthesis approach from GO, Entry IV which involves H_2O_2, HCOOC, and 100 mg of GO (no $NaHCO_3$) represents the most favorable conditions for effective GO fragmentation. Under these conditions, the *in situ* generation of the strong oxidizing pair H_2O_2/HCOOH derived from performic acid is facilitated.[49,50] This oxidative system is well-documented to perform optimally under acidic conditions.[51,52] Importantly, no radical scavengers are present in this system, allowing hydroxyl radicals ($^{\bullet}OH$), critical agents in oxidative cleavage, to remain active and enable the top-down breakdown of GO into g-CQDs.[53] Still, the post-reaction solution from Entry IV shows very limited g-CQD formation, as evidenced by the near absence of fluorescence. In contrast, Entry I, which is similar to Entry IV but includes $NaHCO_3$, shifts the environment toward alkaline conditions and introduces a known hydroxyl radical scavenger.[54,55] This combination significantly suppresses the top-down oxidation of GO however the formation of g-CQDs under conditions containing $NaHCO_3$

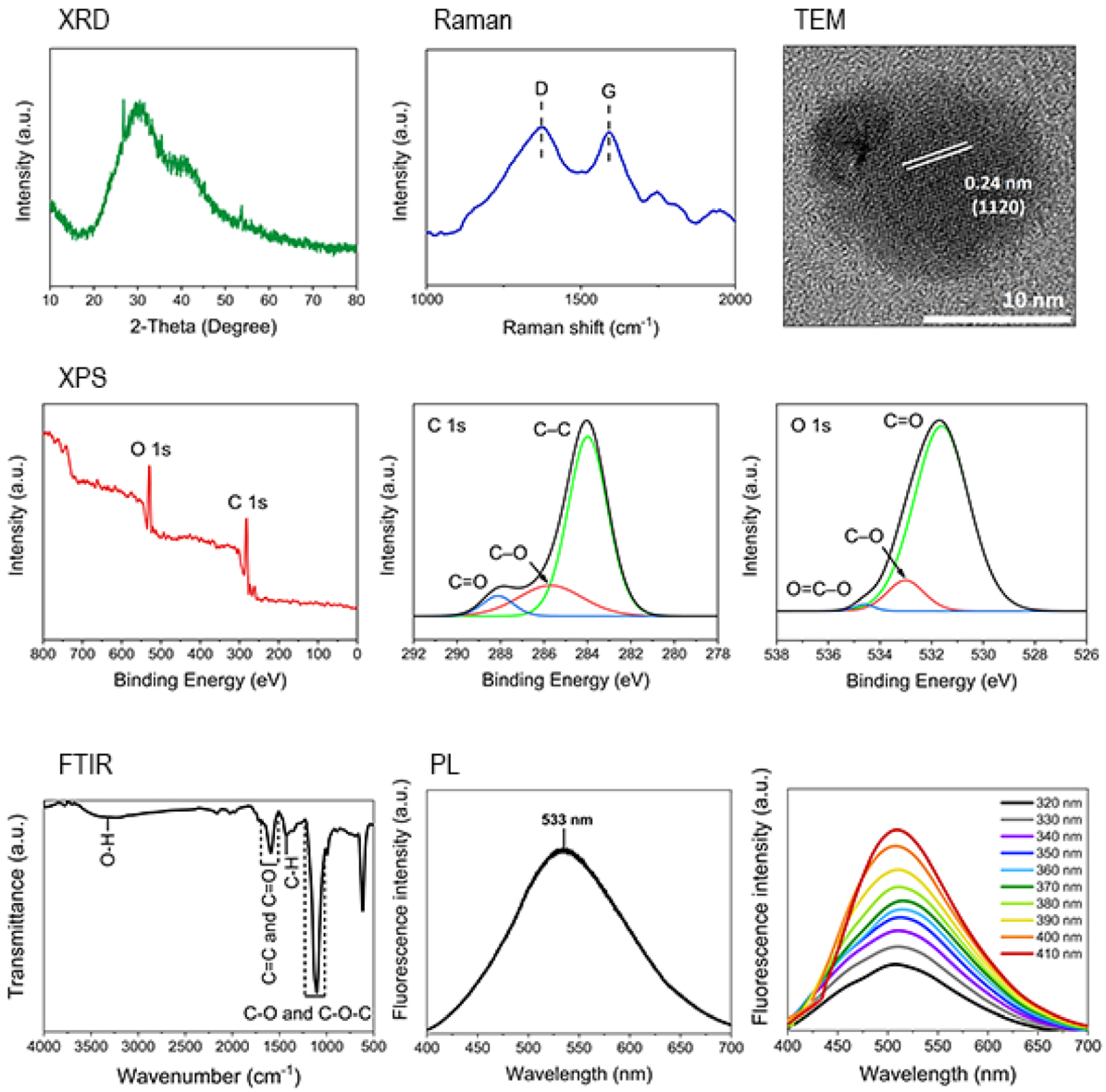

Fig. 3 Characterization of the synthesized g-CQDs by XRD, Raman, TEM, XPS, FT-IR, and PL.

Table 2 Comparison of various conventional bottom-up synthesis methods

Method	Precursors	Others	Reaction time	Condition	Ref.
Hydrothermal	Citric acid	Thiourea	4 h	160 °C	19
		Urea	8 h	160 °C	
	Citric acid	EDA	5–8 h	140–190 °C	64
	Citric acid	NaOH	4 h	160 °C	60
	1,3,6-Trinitropyrene	NaOH	10 h	200 °C	65
	Citric acid	Urea	1 h	180 °C	63
	Nitrilotriacetic acid		4 h	250 °C	66
	Citric acid	Histidine	3 h	200 °C	22
Pyrolysis	Citric acid	BPEI	3 h	200 °C	18
	Melamine powder		72 h	1000 °C	26
Carbonization	Ethylene glycol		24 h	220 °C	67
	Acetone		24 h	220 °C	
	Toluene		24 h	220 °C	
	Dimethylformamide		24 h	220 °C	
	Glycerol		24 h	220 °C	
	Ethylenediamine		24 h	220 °C	
Microwave-assisted	1,3,6-Trinitropyrene	Hydrazine hydrate	3 min	200 °C	29
	Glucosamine	Thiourea	40 min	450 W	28
	Sodium citrate	Triethanolamine	2 min	750 W	68
	Glucose	Ethylene glycol	9 min	800 W	69
Electrochemical	*o*-Phenylenediamine		1 h	500 V	27
Graphene oxide vacancies-assisted low temperature synthesis	Carbonic acid	GO	1 h	72 °C	This work

is markedly higher. This observation suggests that the formation of CQDs in the system does not proceed through direct top-down fragmentation of GO but instead arises from reactions occurring at *in situ* generated vacancy sites within the GO structure. These vacancies may act as both nucleation centers and catalytic active sites.

Moreover, when the amount of GO was decreased to 10 mg (Entry V), only weak luminescence was observed. This stemmed from a reduced graphene oxide vacancies content, which induced, consequently, the number of nucleation sites on graphene oxide vacancies decreased, leading to lower g-CQD production. The role of graphene oxide vacancies as the nucleation site for g-CQD formation was further confirmed when graphite was used as a substitute for GO (Entry VI), where no luminescence was observed. This is likely due to the strongly ordered sp^2 hybridization structure of graphite, which requires harsh chemical treatments or aggressive conditions to generate vacancies. These findings highlight the essential role of GO vacancy sites, particularly as catalytic centers that facilitate the conversion of carbon-containing species (*e.g.*, H_2CO_3) into CQDs, not just the nucleation sites for growing graphitic carbon.

The synthesized g-CQDs were separated out by dialysis and freeze drying and further characterized by XRD, Raman, TEM, XPS, FT-IR, and PL. The characterization results are provided in Fig. 3. The graphitic structure of g-CQDs was confirmed by the XRD result showing broad peak corresponding to the (002) plane of disordered graphite[56,57] and the Raman spectra displaying two prominent peaks at 1373 and 1590 cm^{-1}, corresponding to the D and G bands, which are attributed to disordered and ordered graphitic structures, respectively.[56,58,59] The TEM image also reveals a lattice spacing of 0.24 nm, corresponding to the (1120) crystal plane of graphite.[24,25,60] Surface functional groups of the synthesized g-CQDs characterized by FT-IR and XPS indicate that g-CQDs contain –OH and –COOH functional groups in addition to C–C, C–O, and C=O bonds.[58,59,61] The PL spectra of the dialyzed solution, excited at 360 nm, exhibited maximum emission at 533 nm. These result align with Liu *et al.*,,[62] where GQDs synthesized from a reaction between triethylenetetramine (TETA) and *p*-benzoquinone displayed strong yellow luminescence, with a PL spectrum maximum emission at 543 nm. The excitation-independence of the dialyzed solution at various excitation wavelengths indicates that size and surface state of g-CQDs are uniform.[19,63] The advantages of the present low-temperature, rapid synthesis process for g-CQDs, compared to conventional bottom-up methods, are clearly demonstrated in Table 2.

Fabrication of GNPs/g-CQDs-epoxy composites

The series of epoxy composites containing GNPs and/or g-CQDs was prepared by mixing g-CQDs and/or GNPs, at various loading ratios, as detailed in Table 3, with epoxy resin dissolved in acetone. The mixture was then sonicated at 60 °C for 2 h. Subsequently, the solvent was removed by drying the mixture at 110 °C. After cooling to room temperature, an appropriate amount of hardener was added, followed by mechanical stirring for 1 h and degassing for 30 min. The resulting mixture was then cast into a silicone mold and pre-cured at 80 °C for 2 h, followed by post-curing at 150 °C for 2 h.

Morphology of GNPs/g-CQDs-epoxy composite

The morphology of GNPs, g-CQDs, and GNPs/g-CQDs hybrid fillers are depicted as SEM images in Fig. 4. The GNP sheets

Table 3 Composition of GNPs-epoxy, g-CQDs-epoxy, and GNPs/g-CQDs-epoxy composites

Sample	GNPs loading (wt%)	g-CQDs loading (wt%)
Pristine epoxy	—	—
10gCQD	—	10
5GNP	5	—
7GNP	7	—
10GNP	10	—
5GNP/10gCQD	5	10
7GNP/10gCQD	7	10
10GNP/10gCQD	10	10
10GNP/20gCQD	10	20

display a smooth, flat structure (Fig. 4(a)), while Fig. 4(b) reveals thin, curved sheets forming a three-dimensional (3D) network through the self-assembly of g-CQDs. Moreover, the abundant surface functional groups of g-CQDs such as –OH and –COOH promote the linking of GNPs through hydrogen bonding and π–π interactions, which contribute to the formation of a three-dimensional network structure.[70] The 3D network structures of GNPs/g-CQDs hybrid filles containing 10 wt% GNPs-10 wt% g-CQDs and 10 wt% GNPs-20 wt% g-CQDs are demonstrated in Fig. 4(c) and (d), respectively. A bunch of wrinkles and curvature of the g-CQDs are observed both on and between the GNP sheets, contributing to a 3D network that enhances dispersibility and reduces stacking of GNP sheets by forming non-covalent functionalization through the adsorption of g-CQDs onto the surface of GNPs.[13,16,71] Furthermore, TEM analysis (Fig. 5) confirms that g-CQDs with an average size of approximately 10 nm are uniformly distributed on the surface and between sheet of GNPs. This result suggests the ability of g-CQDs to induce the 3D network formation of GNPs, which may improve the thermal/electrical conductivity.

The morphology of GNPs-epoxy and GNPs/g-CQDs-epoxy composites was observed through their fractural surfaces by SEM. Fig. 6(a) demonstrates a smooth surface of pristine epoxy, while Fig. 6(b) shows the observation of rougher surface by infusion of g-CQDs in epoxy matrix due to small size of g-CQDs. It was expected that g-CQDs could uniformly disperse on epoxy matrix but could not form 3D network. Comparing between pristine epoxy and 10gCQD, the fractural surface of the former showed a brittle-fracture, while the latter showed a ductile-fracture, suggesting that pristine epoxy is brittle than 10gCQD.[72] Fig. 6(c) exhibit rough, wrinkled and high contrast surface of 5GNP, indicating that there is dispersion of GNPs in epoxy matrix. Epoxy composites containing GNPs loading more than 5 wt%. In Fig. 6(g and e) show denser and more packed of GNPs, but there is no difference between 7 wt% and 10 wt% loading of GNPs. Fig. 6(d, f, and h) show rougher surface regions in the composites containing 10 wt% g-CQDs of 5GNP/10gCQD, 7GNP/10gCQD, and 10GNP/10gCQD, respectively. This roughness, similar to that observed in Fig. 6(b), is attributed to interactions between g-CQDs and the epoxy matrix, as well as the wrinkles and curvatures of g-CQDs on GNPs surface observed in Fig. 6(c and d). This series of findings indicates that g-CQDs can formed 3D network with GNPs in both epoxy and non-epoxy system.

A SEM image of fracture surface of 10GNP/20gCQD is presented in Fig. 7(a). Compared to Fig. 6(h), no significant difference is observed between the composites containing 10 wt% and 20 wt% of g-CQDs in the GNPs-epoxy matrix. Fig. 7(b–e) presents the EDX elemental mapping, with Fig. 7(e)

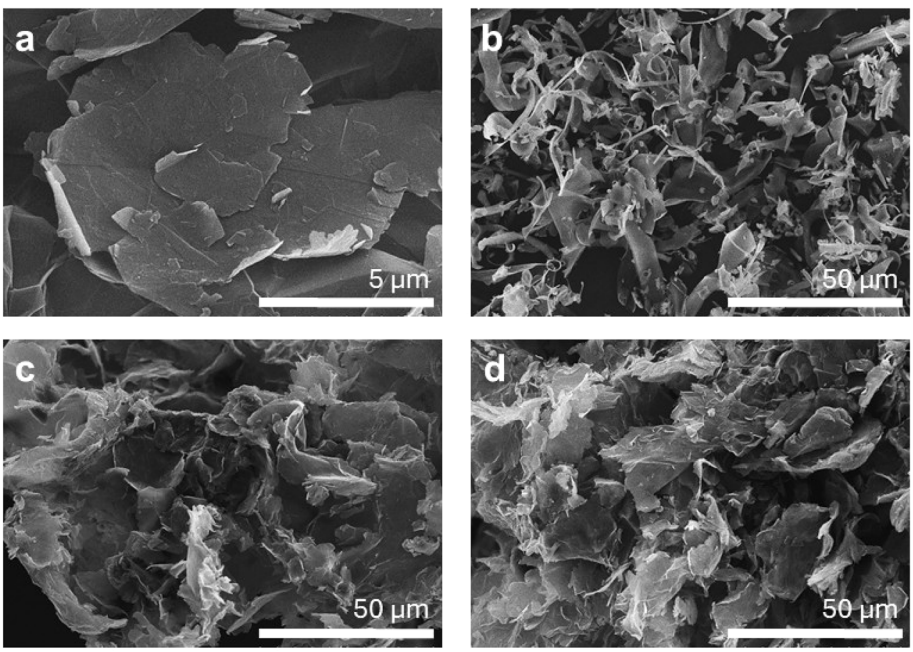

Fig. 4 SEM surface morphology image of (a) GNPs, (b) g-CQDs, and hybrid filler (c) 10 wt% GNPs-10 wt% g-CQDs, and (d) 10 wt% GNPs-20 wt% g-CQDs.

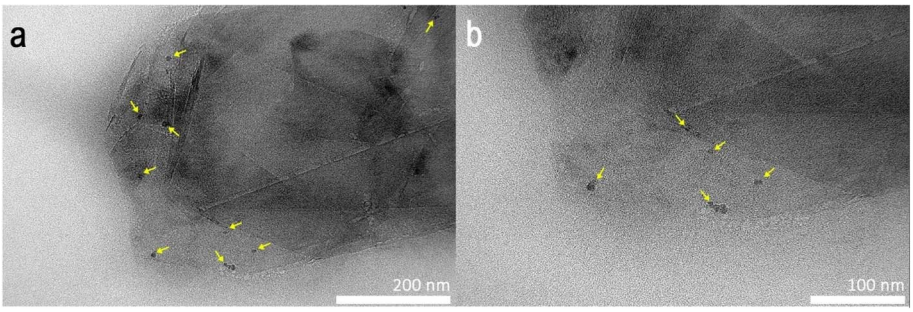

Fig. 5 TEM images showing the adsorption of g-CQDs onto the surface of GNPs at (a) 600 00× and (b) 1 000 00× magnification.

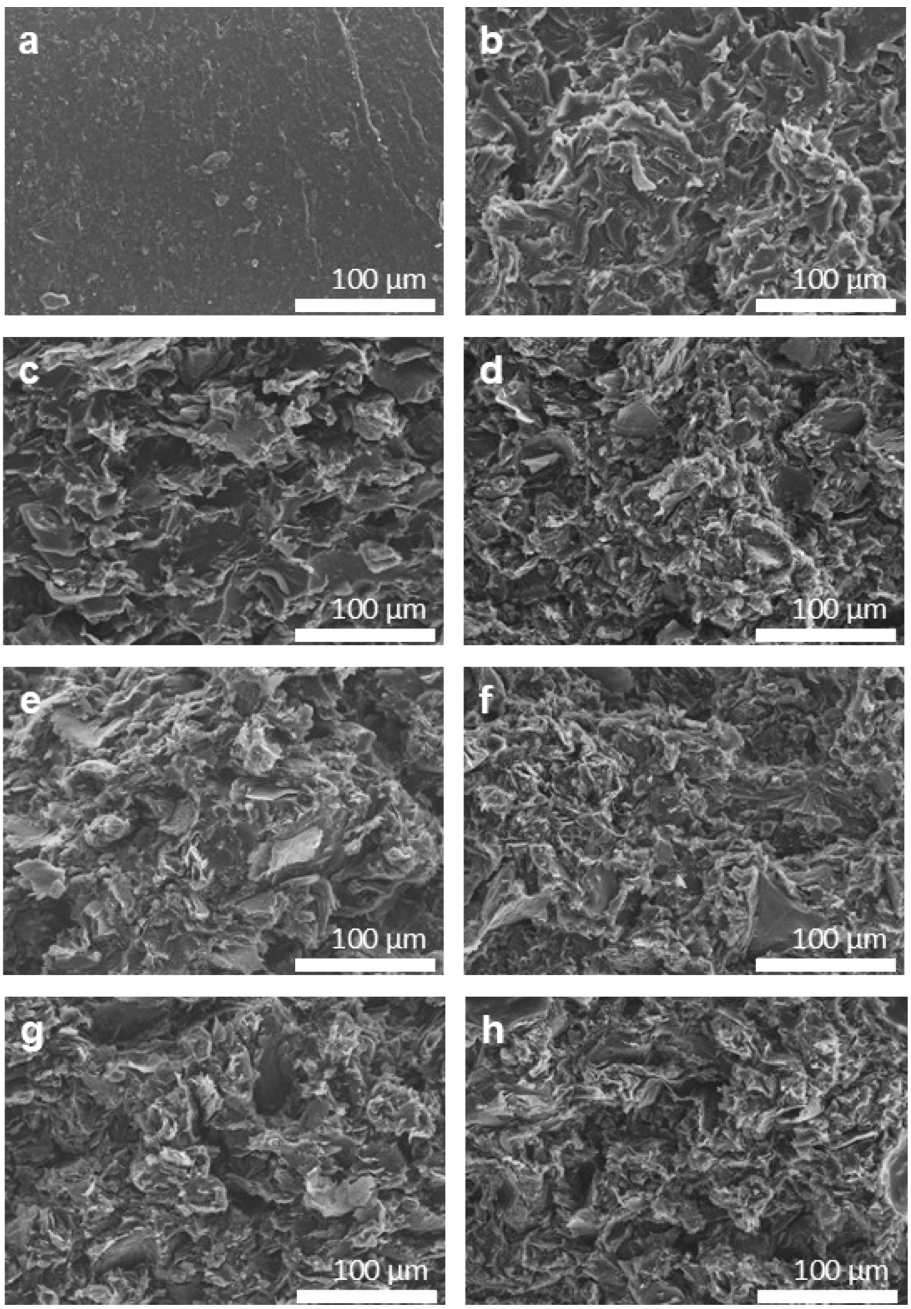

Fig. 6 SEM images of fracture surface (a) pristine epoxy, (b) 10gCQD, (c) 5GNP, (d) 5GNP/10gCQD, (e) 7GNP, (f) 7GNP/10gCQD, (g) 10GNP, and (h) 10GNP/10gCQD.

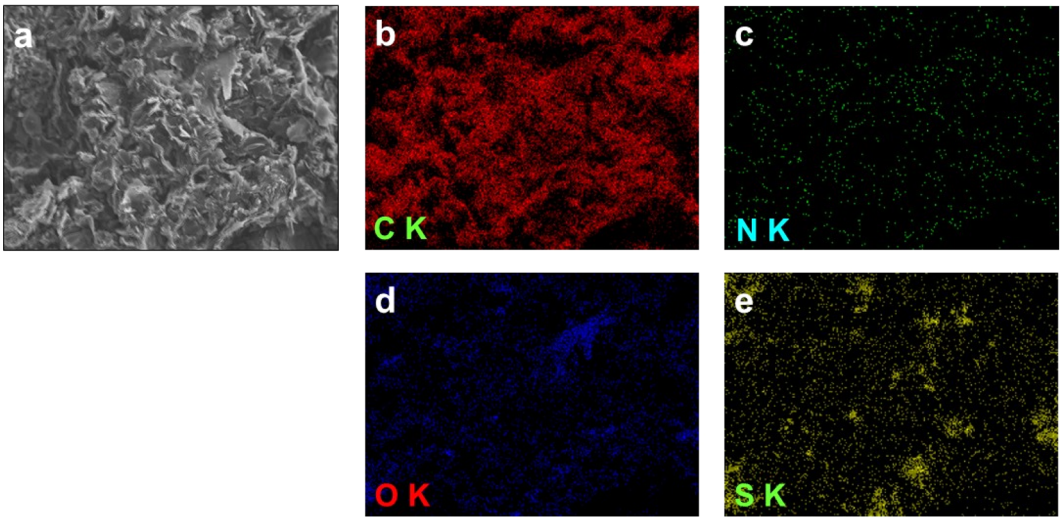

Fig. 7 (a) SEM image of 10GNP/20gCQD, EDX of (b) C, (c) N, (d) O, and (e) S.

specifically highlighting S element, attributed to impurities in the g-CQDs. These impurities appear aggregated and scattered throughout the matrix. However, the SEM-EDX results indicates that g-CQDs are well-dispersed within the epoxy matrix and contribute to the formation of a continuous conductive network. This finding is consistent with the 3D network formation observed between GNPs and g-CQDs in the absence of epoxy matrix (Fig. 4(d)).

Thermal and electrical properties of GNPs/g-CQDs-epoxy composites

The thermal conductivity of GNPs-epoxy composites was reported in several research articles.[6,7,9,73] As expected from the references, the thermal conductivity was increased with increasing GNPs loading, as shown in Fig. 8(a). The thermal conductivity of GNPs-epoxy increases by 100% and 150% of 5GNP and 7GNP respectively, with the maximum value of 0.70 W (m K)$^{-1}$ at 10 wt% of GNPs, which increased by 191.7% compared to pristine epoxy (0.24 W (m K)$^{-1}$). It notices that the thermal conductivity of epoxy composites highly depends on the intrinsic thermal conductivity of fillers, size, shape, and filling amount of the fillers, and the degree of the dispersion of fillers in epoxy matrix.[74] The thermal energy from heat sources can continuously transferred through the vibration of well-ordered sp^2 hybridization of carbon–carbon bonds until it reaches the opposite side of GNPs.[75] When GNPs loading increased, the GNP sheets tend to have good contacts with each other to create the thermally conductive network, reducing the phonon-scattering and thermal interface resistance.[76,77] The incorporation of 10 wt% g-CQDs into pristine epoxy resulted in a slight increase in thermal conductivity to 0.25 W (m K)$^{-1}$ compared to pristine epoxy. As shown in the SEM image (Fig. 6(b)) no 3D network was observed within the epoxy composite, indicating the absence of a continuous thermally conductive pathway. This is attributed to the well-dispersed yet isolated nature of g-CQDs within the epoxy matrix, preventing the formation of an interconnected conductive network.

Upon incorporation of 10 wt% of g-CQDs into GNPs-epoxy composites resulted in a thermal conductivity increase by 16.67% and 18.33% for 5GNP/10gCQD and 7GNP/10gCQD, respectively, compared to 5GNP and 7GNP. The maximum thermal conductivity of 0.93 W (m K)$^{-1}$ was achieved for 10GNP/10gCQD, representing a 32.86% improvement compared to 10GNP. In contrast to the filled epoxy composite with g-CQDs only, the series of results demonstrated that incorporating g-CQDs into GNPs-epoxy composites exhibits a synergistic effect of hybrid fillers with different sizes. The nanoscale size of g-CQDs not only enables good dispersion within the epoxy matrix but also allows them to fill the gaps between GNP sheets, creating effective thermal conductive networks. Fig. 8(b) shows the thermal conductivity of g-CQDs-filled samples. By increasing the g-CQDs loading to 20 wt% further enhanced the thermal conductivity of 10GNP/20gCQD to 1.05 W (m K)$^{-1}$, representing a 50.0% increase compared to 10GNP. This indicates that the thermally conductive network becomes more robust as the g-CQDs loading increases.

The electrical conductivity of GNPs/g-CQDs-epoxy composites was determined by Van Der Pauw method using Keithley 2182A nanovoltmeter is suitable for low resistance materials, only 10GNP can detect the voltage, then the 10GNP/10gCQD and 10GNP/20gCQD were chosen to study effect of g-CQDs infused. The result is shown in Fig. 8(b). The electrical conductivity of the 10GNP-filled sample is 1.12×10^{-5} S m^{-1}, increased by 7 orders of magnitude compared to insulating epoxy (approximately 10^{-12} S m^{-1}).[74] Similar to the thermal conductivity, electrically conductive network is formed by increasing GNPs loading as observed by SEM in Fig. 6(c, e, and g). By infusing 10 and 20 wt% of g-CQDs, the electrical conductivity increased to 9.01×10^{-3} and 1.86×10^{-2} S m^{-1}, respectively, representing increments of 9 and 10 orders of magnitude. The electrical conductivity of the GNP/g-CQDs epoxy composites in this work (10^{-2} to 10^{-3} S m^{-1}) is considered relatively high compared to other GNP-based system reported in the literature, where electrical conductivities typically range from 10^{-6} to 10^{-4} S cm^{-1}, depending on the

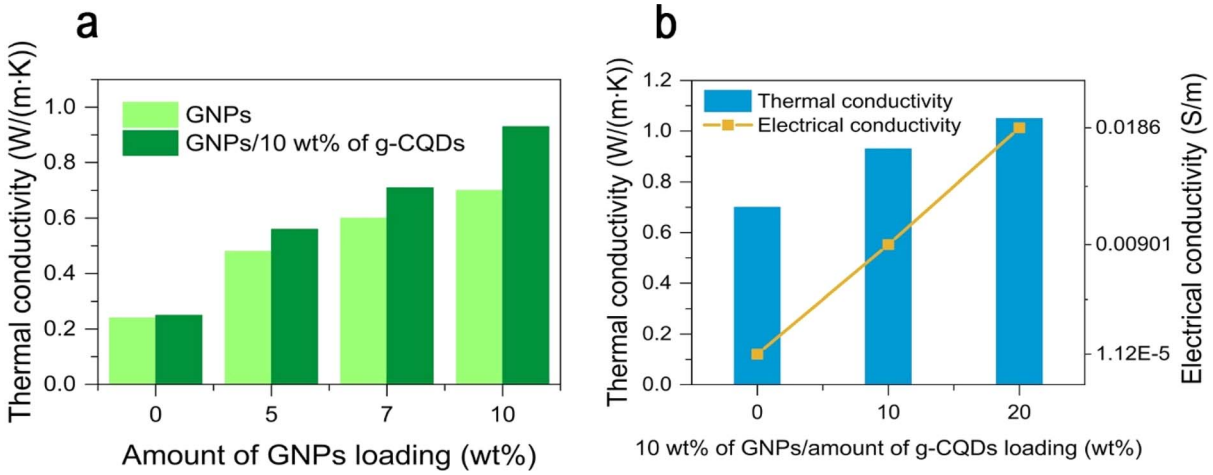

Fig. 8 Thermal conductivity of (a) GNPs-epoxy composites with various GNPs loadings (0, 5, 7 and 10 wt%) with 10 wt% of g-CQDs, (b) thermal and electrical conductivity of GNPs/g-CQDs-epoxy composites with amount of g-CQDs loading of 0, 10, and 20 wt% on 10 wt% of GNPs.

particle size, surface area, and loading amount of GNPs.[78,79] However, the limited increase in electrical conductivity with increasing GNP content was primarily attributed to defect formation and partial agglomeration of the GNPs. The synergistic effects of GNPs/g-CQDs hybrid nanofillers on enhancing thermal and electrical conductivity of epoxy composites are in line with other carbon-based hybrid *e.g.*, the use of CNTs and GNPs hybrid fillers that provided superior performance compared to single one. The highest thermal conductivity was achieved at a CNT : GNP ratio of 20 : 80, while the highest electrical conductivity was observed at a reversed ratio of 80 : 20, with a total filler loading of 8 wt%. In this study, the synthesized g-CQDs demonstrate the ability to prevent the restacking of GNPs, thereby facilitating the formation of a thermally and electrically conductive network. This behavior is comparable to the work of Wan *et al.*,[12] using surfactant-assisted methods to reduce graphene stacking and enhance compatibility with epoxy resins by adsorbing amphiphilic surfactants containing both hydrophilic and hydrophobic groups onto graphene surfaces. Likewise, He *et al.*[13] reported strong adsorption of GQDs onto graphene surfaces, with GQDs behaving as amphiphilic molecules due to their simultaneous hydrophilic and hydrophobic characteristics. g-CQDs not only can absorb on the surface of GNPs to form electrically conductive networks with surrounding particles, but can also decrease the distances among GNP sheets, when GNPs come closer to each other in a few nanometers, electron can hop or tunnel from one GNP sheet to another, resulting in drastic improve in electrical conductivity.[80,81] The synergistic interaction between g-CQDs and GNPs in this study contributed to significant improvements in both thermal and electrical conductivities.

Conclusions

In this study, bottom-up synthesis of g-CQDs was successfully achieved *via* a graphene oxide vacancies-assisted low temperature synthesis, employing H_2CO_3 as the carbon precursor. The reaction was carried out in a simple beaker-type reactor under ambient pressure at 72 °C. Graphene oxide vacancies served as both catalytic sites and nucleation centers for g-CQD formation, enabling the process to complete within 1 hour. The dialyzed g-CQD solution exhibited strong yellow luminescence under UV light, while the freeze-dried g-CQDs self-assembled into a three-dimensional (3D) network structure. Remarkably, g-CQDs also induced the 3D network formation of GNPs in both epoxy and non-epoxy systems, promoting the development of thermally and electrically conductive networks. As a result, the thermal conductivity of epoxy composites containing 10 wt% GNPs and 20 wt% g-CQDs increased to 1.05 W (m K)$^{-1}$, while electrical conductivity improved by 10 orders of magnitude. This synthesis approach is simple, eco-friendly, energy-efficient, and scalable, and highlights the synergistic role of g-CQDs in enhancing the 3D network structure of GNPs.

Data availability

Data for this article are available at the link **https://www.drive.google.com/drive/folders/1RmtXpYSiQrbY0cr9a5ElSf3soLB5033Y?usp=drive_link**.

Conflicts of interest

There are no conflicts to declare.

Acknowledgements

The R4Ent scholarship for T. J. from Chulalongkorn University and the Second Century Fund (C2F) is gratefully acknowledged. The authors would like to thank the CrystalLyte Co., Ltd, for the partial financial support of this research. This work was also partly supported by JST-CREST (JPMJCR24S6 to R. S.) and JST-FOREST (JPMJFR203F to R. S.).

References

1 P. Goli, *et al.*, Graphene-enhanced hybrid phase change materials for thermal management of Li-ion batteries, *J. Power Sources*, 2014, **248**, 37–43.
2 H. Wang, *et al.*, Electrical and mechanical properties of antistatic PVC films containing multi-layer graphene, *Composites, Part B*, 2015, **79**, 444–450.
3 J. Zhang, *et al.*, Improvement in anti-static property and thermal conductivity of epoxy resin by doping graphene, *IEEE Trans. Dielectr. Electr. Insul.*, 2020, **27**(2), 542–548.
4 T.-H. Han, *et al.*, Graphene-based flexible electronic devices, *Mater. Sci. Eng., R*, 2017, **118**, 1–43.
5 P. Cataldi, A. Athanassiou and I. Bayer, Graphene Nanoplatelets-Based Advanced Materials and Recent Progress in Sustainable Applications, *Appl. Sci.*, 2018, **8**(9), 1438.
6 S. Chandrasekaran, C. Seidel and K. Schulte, Preparation and characterization of graphite nano-platelet (GNP)/epoxy nano-composite: Mechanical, electrical and thermal properties, *Eur. Polym. J.*, 2013, **49**(12), 3878–3888.
7 J. Gu, *et al.*, Functionalized graphite nanoplatelets/epoxy resin nanocomposites with high thermal conductivity, *Int. J. Heat Mass Transfer*, 2016, **92**, 15–22.
8 J. A. King, *et al.*, Mechanical properties of graphene nanoplatelet/epoxy composites, *J. Appl. Polym. Sci.*, 2012, **128**(6), 4217–4223.
9 R. Moriche, *et al.*, Thermal conductivity and lap shear strength of GNP/epoxy nanocomposites adhesives, *Int. J. Adhes. Adhes.*, 2016, **68**, 407–410.
10 A. Caradonna, *et al.*, Electrical and Thermal Conductivity of Epoxy-Carbon Filler Composites Processed by Calendaring, *Materials*, 2019, **12**(9), 1522.
11 H.-Y. Zhao, *et al.*, Efficient Preconstruction of Three-Dimensional Graphene Networks for Thermally Conductive Polymer Composites, *Nano-Micro Lett.*, 2022, **14**(1), 129.
12 Y.-J. Wan, *et al.*, Improved dispersion and interface in the graphene/epoxy composites *via* a facile surfactant-assisted process, *Compos. Sci. Technol.*, 2013, **82**, 60–68.
13 P. He, *et al.*, Processable Aqueous Dispersions of Graphene Stabilized by Graphene Quantum Dots, *Chem. Mater.*, 2015, **27**(1), 218–226.
14 G. He, *et al.*, Synergetic enhancement of thermal conductivity for highly explosive-filled polymer composites through hybrid carbon nanomaterials, *Polym. Compos.*, 2018, **39**(S3), E1452–E1462.
15 J. Jyoti, *et al.*, Mechanical, electrical and thermal properties of graphene oxide-carbon nanotube/ABS hybrid polymer nanocomposites, *J. Polym. Res.*, 2020, **27**(9), 282.
16 A. Navidfar and L. Trabzon, Analytical modeling and experimentally optimizing synergistic effect on thermal conductivity enhancement of polyurethane nanocomposites with hybrid carbon nanofillers, *Polym. Compos.*, 2021, **42**(2), 944–954.
17 Y.-L. Zhang, *et al.*, Graphitic carbon quantum dots as a fluorescent sensing platform for highly efficient detection of Fe 3+ ions, *RSC Adv.*, 2013, **3**(11), 3733–3738.
18 Y. Dong, *et al.*, Polyamine-functionalized carbon quantum dots for chemical sensing, *Carbon*, 2012, **50**(8), 2810–2815.
19 D. Qu, *et al.*, Highly luminescent S, N co-doped graphene quantum dots with broad visible absorption bands for visible light photocatalysts, *Nanoscale*, 2013, **5**(24), 12272–12277.
20 P. Tian, *et al.*, Graphene quantum dots from chemistry to applications, *Mater. Today Chem.*, 2018, **10**, 221–258.
21 Y. Yan, *et al.*, Recent Advances on Graphene Quantum Dots: From Chemistry and Physics to Applications, *Adv. Mater.*, 2019, **31**(21), e1808283.
22 H. Qiu, *et al.*, Microwave synthesis of histidine-functionalized graphene quantum dots/Ni-Co LDH with flower ball structure for supercapacitor, *J. Colloid Interface Sci.*, 2020, **567**, 264–273.
23 T. T. Win, *et al.*, Innovative GQDs and supra-GQDs assemblies for developing high strength and conductive cement composites, *Constr. Build. Mater.*, 2024, **421**, 135693.
24 J. R. Seibert, *et al.*, Infusion of graphene quantum dots to modulate thermal conductivity and dynamic mechanical properties of polymers, *Polymer*, 2019, **185**, 121988.
25 D. Zhang, *et al.*, D-GQDs modified epoxy resin enhances the thermal conductivity of ALN/epoxy resin thermally conductive composites, *Polymers*, 2021, **13**(23), 4074.
26 C. Zhu, *et al.*, Negative induction effect of graphite N on graphene quantum dots: tunable band gap photoluminescence, *J. Mater. Chem. C*, 2015, **3**(34), 8810–8816.
27 L. Tian, *et al.*, Green, simple and large scale synthesis of N-doped graphene quantum dots with uniform edge groups by electrochemical bottom-up synthesis, *RSC Adv.*, 2016, **6**(86), 82648–82653.
28 M. T. Hasan, *et al.*, Photo-and electroluminescence from nitrogen-doped and nitrogen–sulfur codoped graphene quantum dots, *Adv. Funct. Mater.*, 2018, **28**(42), 1804337.
29 W. Li, *et al.*, Three Minute Ultrarapid Microwave-Assisted Synthesis of Bright Fluorescent Graphene Quantum Dots for Live Cell Staining and White LEDs, *ACS Appl. Nano Mater.*, 2018, **1**(4), 1623–1630.
30 N. M. Tho and T. K. Ha, A theoretical study of the formation of carbonic acid from the hydration of carbon dioxide: a case of active solvent catalysis, *J. Am. Chem. Soc.*, 1984, **106**(3), 599–602.
31 O. Philips'Gloeilampenfabrieken, A method of measuring specific resistivity and Hall effect of discs of arbitrary shape, *Philips Res. Rep.*, 1958, **13**(1), 1–9.
32 T. Ji, *et al.*, The mechanism of the reaction of graphite oxide to reduced graphene oxide under ultraviolet irradiation, *Carbon*, 2013, **54**, 412–418.
33 C. Yu, *et al.*, Engineering nano-porous graphene oxide by hydroxyl radicals, *Carbon*, 2016, **105**, 291–296.
34 X. Yan, *et al.*, Clarifying the Origin of Oxygen Reduction Activity in Heteroatom-Modified Defective Carbon, *Cell Rep. Phys. Sci.*, 2020, **1**(7), 100083.

35 X. Yan, Y. Jia and X. Yao, Defects on carbons for electrocatalytic oxygen reduction, *Chem. Soc. Rev.*, 2018, **47**(20), 7628–7658.
36 Q. Wu, *et al.*, Ultra-dense carbon defects as highly active sites for oxygen reduction catalysis, *Chem*, 2022, **8**(10), 2715–2733.
37 S. Navalon, *et al.*, Active sites on graphene-based materials as metal-free catalysts, *Chem. Soc. Rev.*, 2017, **46**(15), 4501–4529.
38 X. Chen, W.-D. Oh and T.-T. Lim, Graphene- and CNTs-based carbocatalysts in persulfates activation: Material design and catalytic mechanisms, *Chem. Eng. J.*, 2018, **354**, 941–976.
39 M. S. Ahmad and Y. Nishina, Graphene-based carbocatalysts for carbon–carbon bond formation, *Nanoscale*, 2020, **12**(23), 12210–12227.
40 S. Xu, *et al.*, Electric-field-assisted growth of vertical graphene arrays and the application in thermal interface materials, *Adv. Funct. Mater.*, 2020, **30**(34), 2003302.
41 Q. Ni, *et al.*, Rapid synthesis of carbon quantum dot-integrated metal–organic framework nanosheets *via* electron beam irradiation for selective 5-hydroxymethylfurfural electrooxidation, *Adv. Powder Mater.*, 2025, **4**(2), 100267.
42 J. Mao, *et al.*, Realization of a tunable artificial atom at a supercritically charged vacancy in graphene, *Nat. Phys.*, 2016, **12**(6), 545–549.
43 H. L. Mai, *et al.*, The role of vacancies in electric field mediated graphene oxide reduction, *Appl. Phys. Lett.*, 2018, **113**(7), 073103.
44 C. Turley, *et al.*, *Literature Review: Environmental Impacts of a Gradual or Catastrophic Release of CO_2 into the Marine Environment Following Carbon Dioxide Capture*, Report to the UK Department for Environment, 2004.
45 D. Pan, *et al.*, Hydrothermal route for cutting graphene sheets into blue-luminescent graphene quantum dots, *Adv. Mater.*, 2010, **22**(6), 734–738.
46 T. Fan, *et al.*, Controllable size-selective method to prepare graphene quantum dots from graphene oxide, *Nanoscale Res. Lett.*, 2015, **10**, 1–8.
47 Y. Zhao, *et al.*, A facile and high-efficient approach to yellow emissive graphene quantum dots from graphene oxide, *Carbon*, 2017, **124**, 342–347.
48 H. Sun, *et al.*, Synthesis of fluorinated and nonfluorinated graphene quantum dots through a new top-down strategy for long-time cellular imaging, *Chem.–Eur. J.*, 2015, **21**(9), 3791–3797.
49 C. H. W. Hirs, [19] Performic acid oxidation, in *Methods in Enzymology*, Academic Press, 1967, pp. 197–199.
50 W. Ahmad, *et al.*, Oxidative Desulfurization of Petroleum Distillate Fractions Using Manganese Dioxide Supported on Magnetic Reduced Graphene Oxide as Catalyst, *Nanomaterials*, 2021, **11**(1), 203.
51 D. Kiejza, *et al.*, Peracids - New oxidants in advanced oxidation processes: The use of peracetic acid, peroxymonosulfate, and persulfate salts in the removal of organic micropollutants of emerging concern – a review, *Sci. Total Environ.*, 2021, **790**, 148195.
52 N. Ding, *et al.*, Kinetics and mechanisms of bacteria disinfection by performic acid in wastewater: In comparison with peracetic acid and sodium hypochlorite, *Sci. Total Environ.*, 2023, **878**, 162606.
53 H. Fan, *et al.*, Hydroxyl radical-mediated synthesis of carbonyl functionalized graphene quantum dots-like as enzyme mimics with tunable fluorescence emission, *Anal. Chim. Acta*, 2024, **1318**, 342931.
54 G. V. Buxton and A. J. Elliot, *Rate constant for reaction of hydroxyl radicals with bicarbonate ions.* International Journal of Radiation Applications and Instrumentation. Part C, *Radiat. Phys. Chem.*, 1986, **27**(3), 241–243.
55 C. Wu and K. G. Linden, Phototransformation of selected organophosphorus pesticides: roles of hydroxyl and carbonate radicals, *Water Res.*, 2010, **44**(12), 3585–3594.
56 Y. Zhu, *et al.*, Graphitic Carbon Quantum Dots Modified Nickel Cobalt Sulfide as Cathode Materials for Alkaline Aqueous Batteries, *Nano-Micro Lett.*, 2020, **12**(1), 16.
57 M. D. Hossain, *et al.*, Graphitization of low-density amorphous carbon for electrocatalysis electrodes from ReaxFF reactive dynamics, *Carbon*, 2021, **183**, 940–947.
58 J.-J. Yao, *et al.*, 3D nitrogen and boron dual-doped carbon quantum dots/reduced graphene oxide aerogel for advanced aqueous and flexible quasi-solid-state zinc-ion hybrid capacitors, *Rare Met.*, 2023, **42**(7), 2307–2323.
59 J. Li, *et al.*, Three-dimensional nitrogen and phosphorus co-doped carbon quantum dots/reduced graphene oxide composite aerogels with a hierarchical porous structure as superior electrode materials for supercapacitors, *J. Mater. Chem. A*, 2019, **7**(46), 26311–26325.
60 D. Qu, *et al.*, Formation mechanism and optimization of highly luminescent N-doped graphene quantum dots, *Sci. Rep.*, 2014, **4**(1), 5294.
61 Z. Lu, *et al.*, Battery-type Ni-Co-Se hollow microspheres cathode materials enabled by bifunctional N-doped carbon quantum dots with ultrafast electrochemical kinetics for hybrid supercapacitors, *Chem. Eng. J.*, 2022, **450**, 138347.
62 M. L. Liu, *et al.*, Large-scale simultaneous synthesis of highly photoluminescent green amorphous carbon nanodots and yellow crystalline graphene quantum dots at room temperature, *Green Chem.*, 2017, **19**(15), 3611–3617.
63 T. Ogi, *et al.*, Transient nature of graphene quantum dot formation *via* a hydrothermal reaction, *RSC Adv.*, 2014, **4**(99), 55709–55715.
64 J. Gu, *et al.*, Facile synthesis and photoluminescence characteristics of blue-emitting nitrogen-doped graphene quantum dots, *Nanotechnology*, 2016, **27**(16), 165704.
65 L. Wang, *et al.*, Gram-scale synthesis of single-crystalline graphene quantum dots with superior optical properties, *Nat. Commun.*, 2014, **5**(1), 5357.
66 R. Tian, *et al.*, Facile preparation and the stepwise formation mechanistic investigation of gram-scale nitrogen-doped graphene quantum dots, *J. Mater. Chem. C*, 2017, **5**(35), 9174–9180.
67 H. Liu, *et al.*, Direct carbonization of organic solvents toward graphene quantum dots, *Nanoscale*, 2020, **12**(20), 10956–10963.

68 Q. Ren, L. Ga and J. Ai, Rapid Synthesis of Highly Fluorescent Nitrogen-Doped Graphene Quantum Dots for Effective Detection of Ferric Ions and as Fluorescent Ink, *ACS Omega*, 2019, **4**(14), 15842–15848.

69 M. Yao, *et al.*, Transforming glucose into fluorescent graphene quantum dots *via* microwave radiation for sensitive detection of Al 3+ ions based on aggregation-induced enhanced emission, *Analyst*, 2020, **145**(21), 6981–6986.

70 G. Chen, *et al.*, Assembling carbon quantum dots to a layered carbon for high-density supercapacitor electrodes, *Sci. Rep.*, 2016, **6**(1), 19028.

71 P. Govindaraj, *et al.*, Distribution states of graphene in polymer nanocomposites: A review, *Composites, Part B*, 2021, **226**, 109353.

72 M. George and A. Mohanty, Investigation of mechanical properties of graphene decorated with graphene quantum dot-reinforced epoxy nanocomposite, *J. Appl. Polym. Sci.*, 2020, **137**(19), 48680.

73 S. A. Haddadi, *et al.*, Epoxy nanocomposite coatings with enhanced dual active/barrier behavior containing graphene-based carbon hollow spheres as corrosion inhibitor nanoreservoirs, *Corros. Sci.*, 2021, **185**, 109428.

74 S. Liu, *et al.*, A review of extending performance of epoxy resins using carbon nanomaterials, *Composites, Part B*, 2018, **136**, 197–214.

75 N. Burger, *et al.*, Review of thermal conductivity in composites: Mechanisms, parameters and theory, *Prog. Polym. Sci.*, 2016, **61**, 1–28.

76 H. S. Kim, *et al.*, Thermal conductivity of polymer composites with the geometrical characteristics of graphene nanoplatelets, *Sci. Rep.*, 2016, **6**, 26825.

77 S. Jasmee, *et al.*, Interface thermal resistance and thermal conductivity of polymer composites at different types, shapes, and sizes of fillers: A review, *Polym. Compos.*, 2021, **42**(6), 2629–2652.

78 Y. Wang, *et al.*, Enhanced thermal and electrical properties of epoxy composites reinforced with graphene nanoplatelets, *Polym. Compos.*, 2015, **36**(3), 556–565.

79 A. R. Ravindran, *et al.*, Effects of Graphene Nanoplatelet Size and Surface Area on the AC Electrical Conductivity and Dielectric Constant of Epoxy Nanocomposites, *Polymers*, 2018, **10**(5), 477.

80 W. Zhang, A. A. Dehghani-Sanij and R. S. Blackburn, Carbon based conductive polymer composites, *J. Mater. Sci.*, 2007, **42**(10), 3408–3418.

81 X. Xia, *et al.*, A theory of electrical conductivity, dielectric constant, and electromagnetic interference shielding for lightweight graphene composite foams, *J. Appl. Phys.*, 2016, **120**(8), 085102.